Supporting Information for:

Optical pressure sensing in the vacuum and high-pressure ranges using lanthanide-based luminescent thermometer-manometer

Marcin Runowski,[1,2,*] Przemysław Woźny[1] and Inocencio R. Martín[2]

[1]*Adam Mickiewicz University, Faculty of Chemistry, Uniwersytetu Poznańskiego 8, 61-614 Poznań, Poland, *E-mail: runowski@amu.edu.pl*

[2]*Departamento de Física, MALTA Consolider Team, IMN, Universidad de La Laguna, Apdo. Correos 456, E-38200 San Cristóbal de La Laguna, Santa Cruz de Tenerife, Spain*
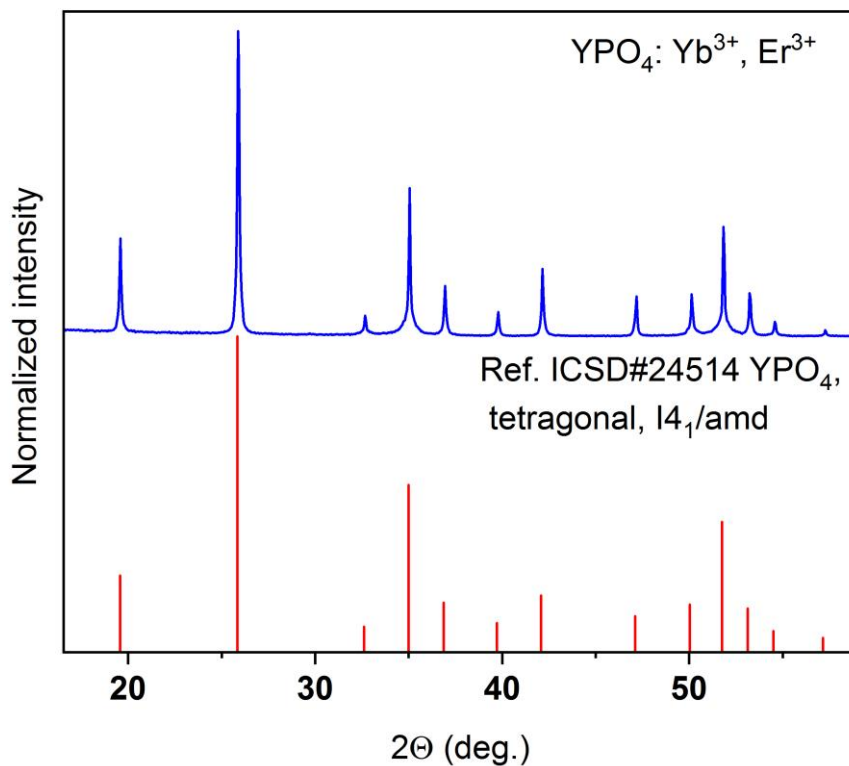
Figure S1. Experimental powder XRD pattern of the YPO_4:Yb^{3+}-Er^{3+} material (top), and the corresponding reference pattern (bottom), from the Inorganic Crystal Structure Database (ICDD#17-0341).

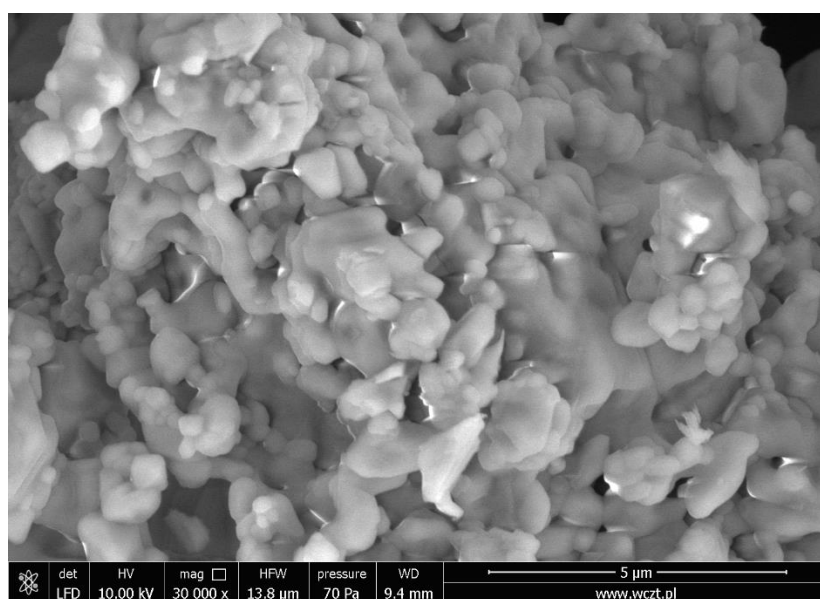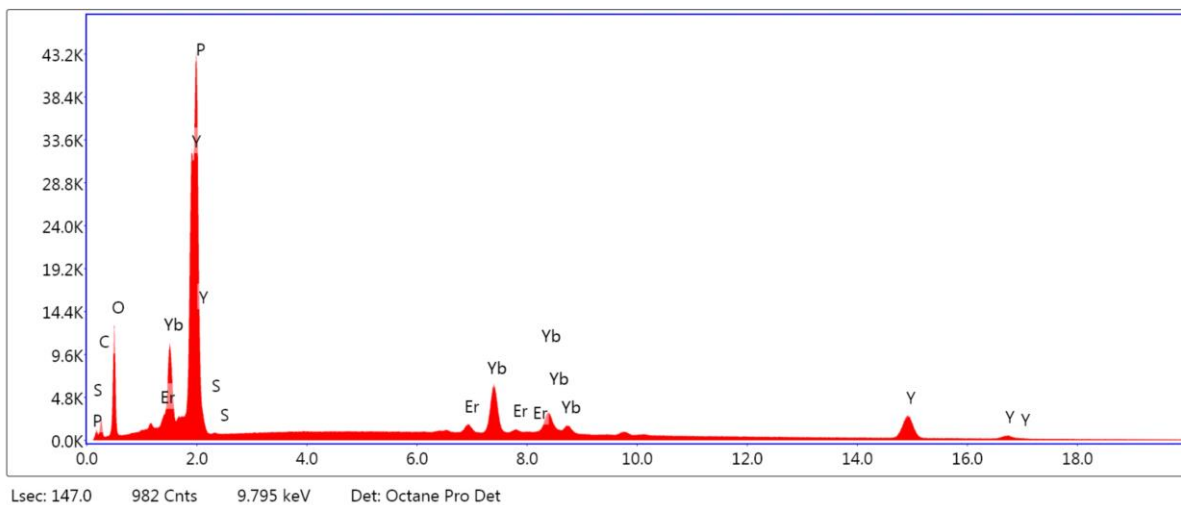**Figure S2.** SEM image of the YPO_4:Yb^{3+}-Er^{3+} material.

Figure S3. EDX spectrum of the YPO$_4$:Yb^{3+}-Er^{3+} material.

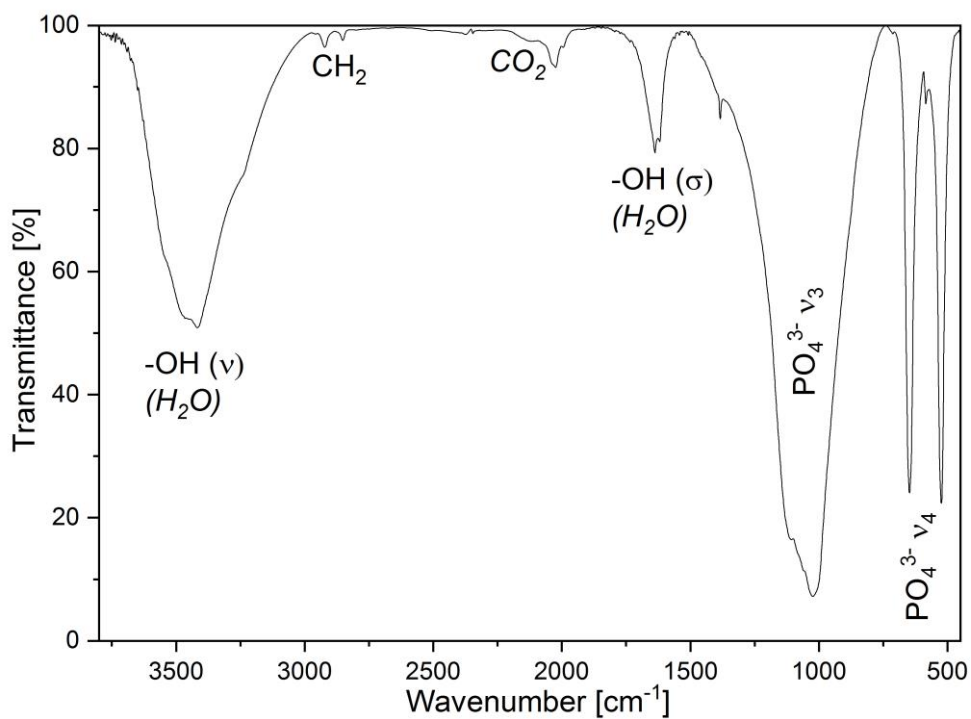**Figure S4.** FT-IR spectrum of the YPO$_4$:Yb^{3+}-Er^{3+} material.

In order to check the reliability of temperature sensing, we have performed repetitive measurements of the LIR parameter, i.e. Er^{3+} band intensity ratio 525/550 nm, by cycling the sample between low and high temperatures (Figure S5). The determined LIR parameter reversibly change with temperature during the performed heating-cooling cycles, confirming thermal stability and reusability of the luminescent thermometer used.
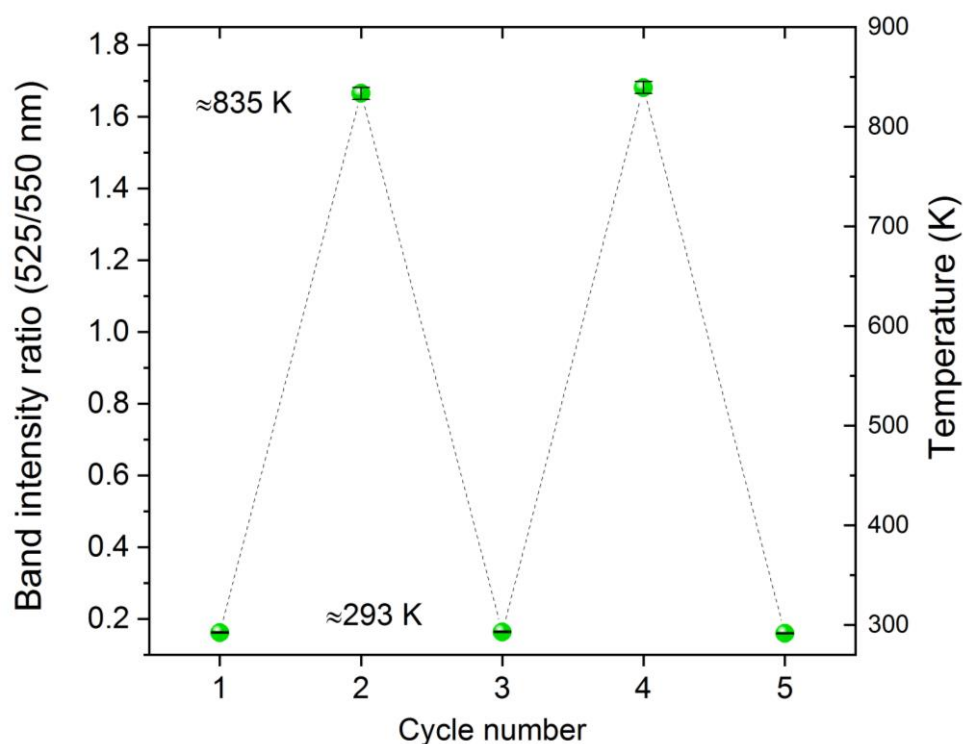

Figure S5. Thermal cycling of the measured LIR parameter (band intensity ratio of Er^{3+}; 525/550 nm), between low and high temperatures, for the YPO$_4$:Yb^{3+}-Er^{3+} sample.

Figure S6 presents relative temperature sensitivity - $S_r(T)$ for the luminescent thermometer used. This parameter is commonly used to quantitatively compare the performance of different optical thermometers, because it is independent of the measuring setup, and shows how the measured thermometric parameter (in this case LIR) changes per 1 K. The $S_r(T)$ parameter is usually expressed in % K^{-1}, and it is determined according to the formula:

$$S_r(T) = 100\% \times \frac{1}{\text{LIR}} \frac{d\text{LIR}}{dT} \tag{S1}$$

At ambient temperature the $S_r(T)$ is around 1.25 %K^{-1}, and continuously decreases to around 0.15 %K^{-1} at about 900 K. The obtained $S_r(T)$ values are similar to the literature data reported elsewhere (the comparison of temperature sensitivity with other reports is presented in Table S1), for different inorganic luminescent thermometers based of Er^{3+} emission.
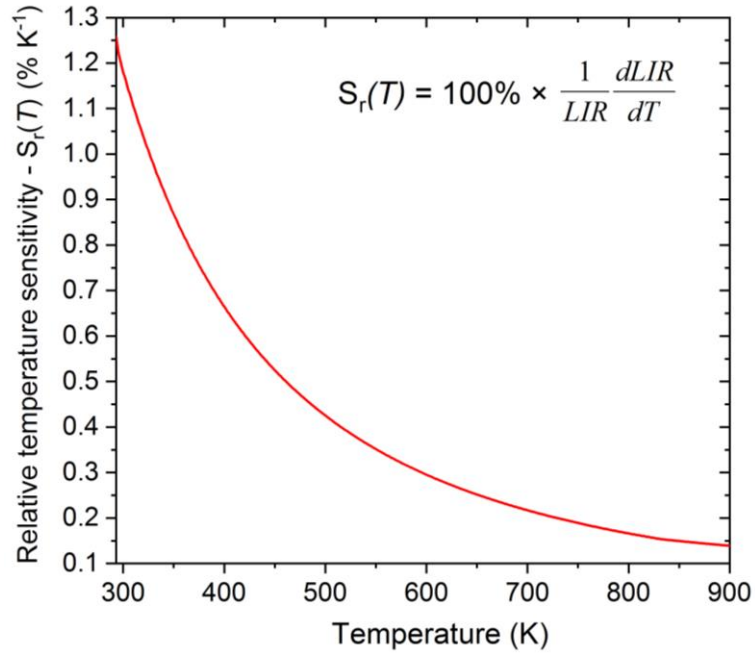

Figure S6. Relative temperature sensitivity – $S_r(T)$ of the YPO$_4$: Yb^{3+}-Er^{3+} optical thermometer as a function of temperature, for temperature sensing with LIR 525/550 nm.

Figure S7 shows the determined temperature resolution, δT (uncertainty of temperature determination), defined as:

$$\delta T = \frac{1}{S_r(T)} \frac{\delta\text{LIR}}{\text{LIR}} \tag{S2}$$

where δLIR is an uncertainty of determination of the LIR parameter. At room temperature the δT is smaller than 1 K. Together with increasing temperature δT gradually increases up to around 7 K around 900 K.

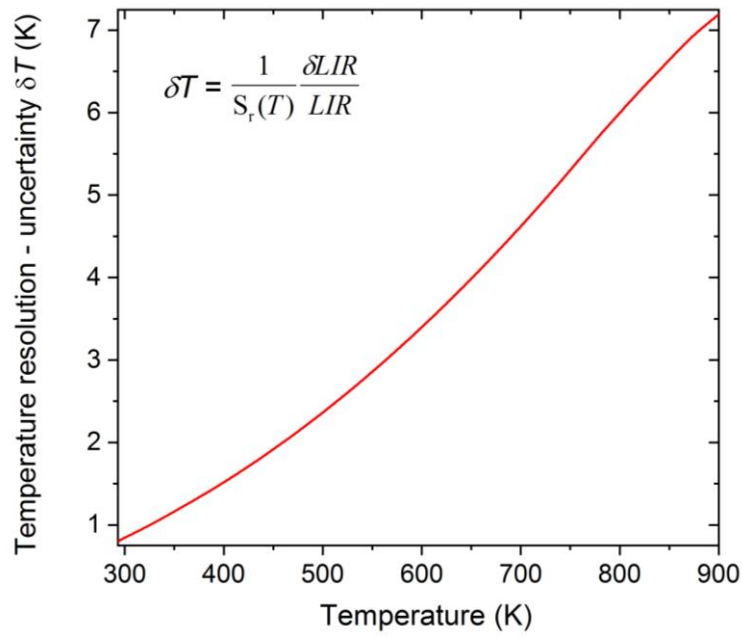$$\delta T = \frac{1}{S_r(T)}\frac{\delta LIR}{LIR}$$

Figure S7. Temperature resolution (δT) of the YPO$_4$:Yb-Er optical thermometer as a function of temperature, for temperature sensing with LIR 525/550 nm.

Table S1 Sensitivity comparison of different inorganic, luminescent (ratiometric) thermometers used for optical temperature sensing, based on the Er^{3+} TCLs (LIR).

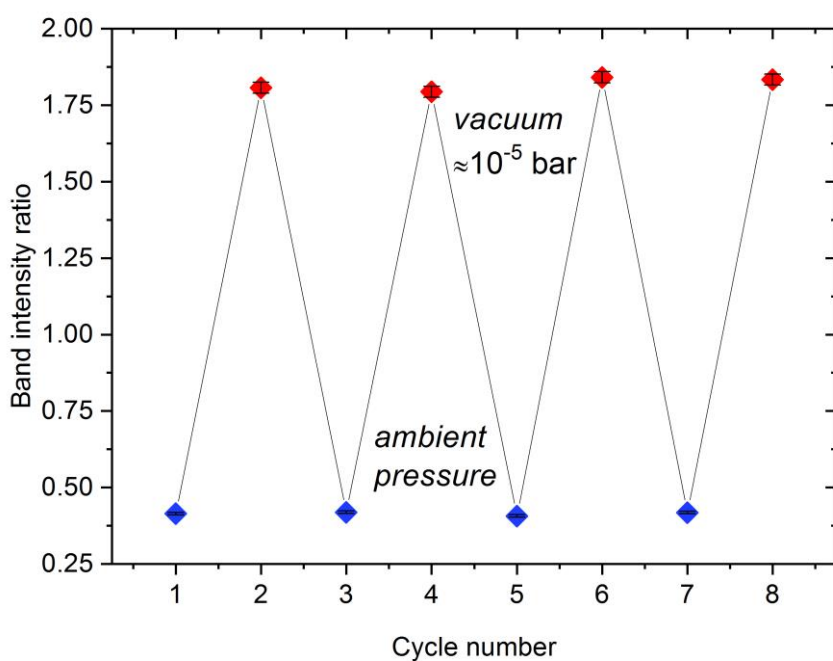| Dopant ions	Host	$S_{r\,max}$ (% K^{-1})	T (K)	T-range (K)	Transitions	λ (nm)	Ref.
Yb^{3+}-Er^{3+}	YF$_3$	1.20	295	295-478	$^2H_{11/2}\rightarrow{}^4I_{15/2}/^4S_{3/2}\rightarrow{}^4I_{15/2}$	525/545	[1]
Yb^{3+}-Nd^{3+}-Er^{3+}	GdOF/SiO$_2$	1.60	260	260-490	$^2H_{11/2}\rightarrow{}^4I_{15/2}/^4S_{3/2}\rightarrow{}^4I_{15/2}$	534/543	[2]
Yb^{3+}-Er^{3+}	SrF$_2$	1.20	298	298-383	$^2H_{11/2}\rightarrow{}^4I_{15/2}/^4S_{3/2}\rightarrow{}^4I_{15/2}$	525/545	[3]
Yb^{3+}-Er^{3+}	Gd$_2$O$_3$	0.85	300	300-900	$^2H_{11/2}\rightarrow{}^4I_{15/2}/^4S_{3/2}\rightarrow{}^4I_{15/2}$	523/548	[4]
Yb^{3+}-Er^{3+}	Tellurite glass	0.53	298	298-473	$^2H_{11/2}\rightarrow{}^4I_{15/2}/^4S_{3/2}\rightarrow{}^4I_{15/2}$	525/548	[5]
Yb^{3+}-Er^{3+}	KBaY(MoO$_4$)$_3$	1.80	250	250-460	$^2H_{11/2}\rightarrow{}^4I_{15/2}/^4S_{3/2}\rightarrow{}^4I_{15/2}$	519/550	[6]
Yb^{3+}-Er^{3+}	SrWO$_4$	0.96	300	300-518	$^2H_{11/2}\rightarrow{}^4I_{15/2}/^4S_{3/2}\rightarrow{}^4I_{15/2}$	525/547	[7]
Yb^{3+}-Er^{3+}	Gd$_2$(MoO$_4$)$_3$	1.34	295	295-660	$^2H_{11/2}\rightarrow{}^4I_{15/2}/^4S_{3/2}\rightarrow{}^4I_{15/2}$	530/550	[8]
Yb^{3+}-Er^{3+}	Bi$_4$Ti$_3$O$_{12}$	1.19	293	293-573	$^2H_{11/2}\rightarrow{}^4I_{15/2}/^4S_{3/2}\rightarrow{}^4I_{15/2}$	530/554	[9]
Yb^{3+}-Er^{3+}	YPO$_4$	1.25	293	293-900	$^2H_{11/2}\rightarrow{}^4I_{15/2}/^4S_{3/2}\rightarrow{}^4I_{15/2}$	525/550	this work

Figure S8. Pressure cycling of the measured LIR parameter (band intensity ratio of Er^{3+}; 525/550 nm), between atmospheric pressure and vacuum ($\approx 2x10^{-5}$ bar).
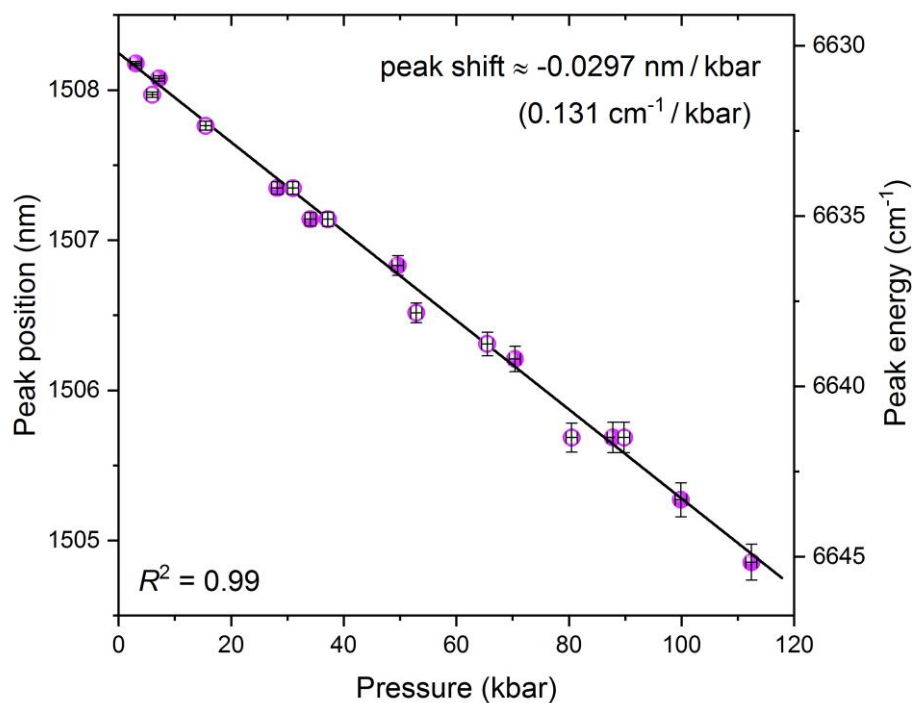

Figure S9. Determined spectral positions of the $^4I_{13/2} \rightarrow {}^4I_{15/2}$ band (Stark sublevel centered at ≈ 1508 nm) of Er^{3+}, as a function of high-pressure; the continues line corresponds to the applied linear fit.

Figure S10. Determined spectral positions of the ${}^4I_{13/2} \rightarrow {}^4I_{15/2}$ band (Stark sublevel centered at ≈1542 nm) of Er^{3+}, as a function of high-pressure; the continues line corresponds to the applied linear fit.
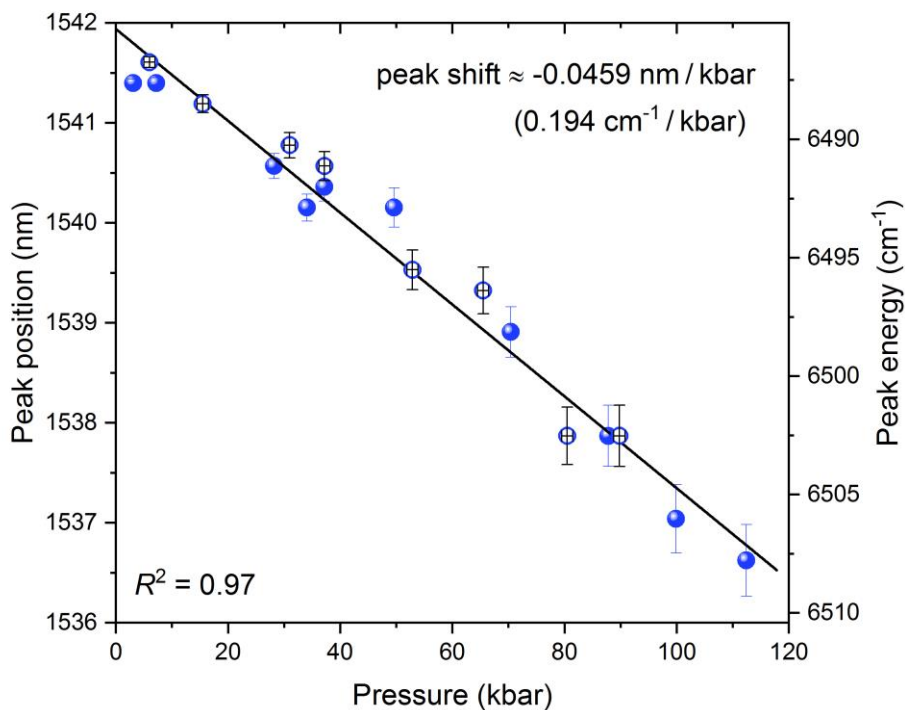

Figure S11. Determined spectral positions of the ${}^4I_{13/2} \rightarrow {}^4I_{15/2}$ band (Stark sublevel centered at ≈1565 nm) of Er^{3+}, as a function of high-pressure; the continues line corresponds to the applied linear fit.
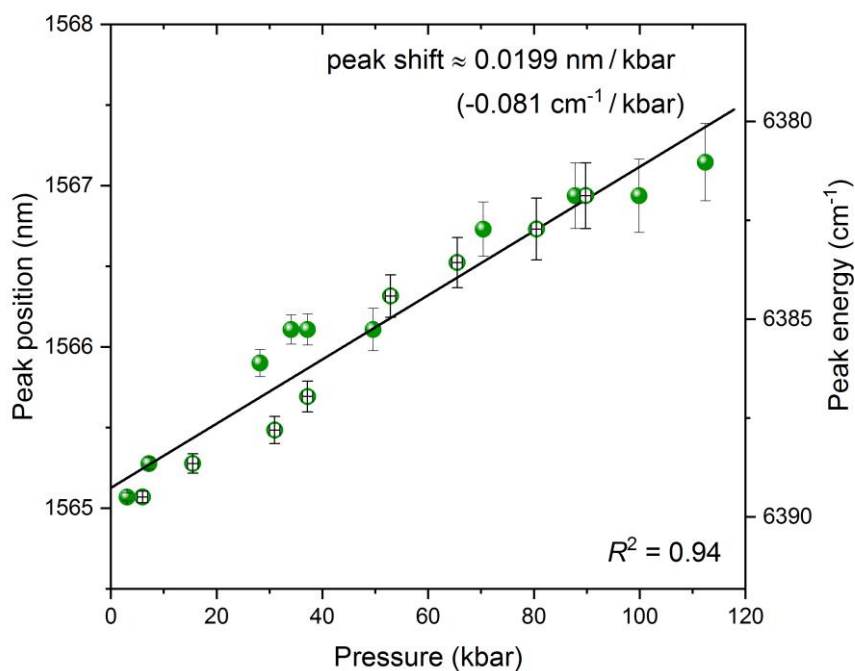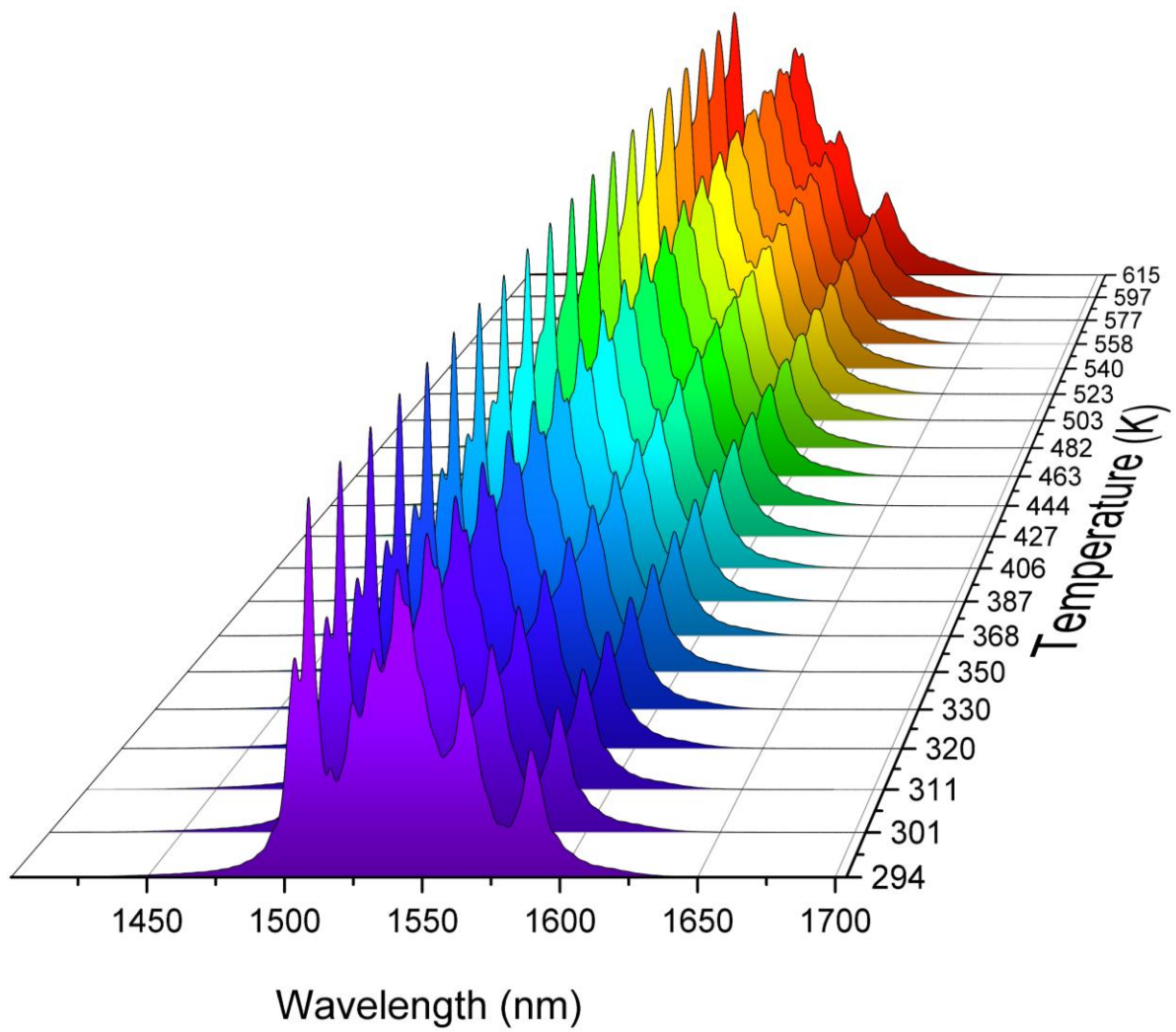
Figure S12. NIR emission spectra of the YPO$_4$:Yb^{3+}-Er^{3+} material (λ_{ex} = 975 nm), measured as a function of temperature.
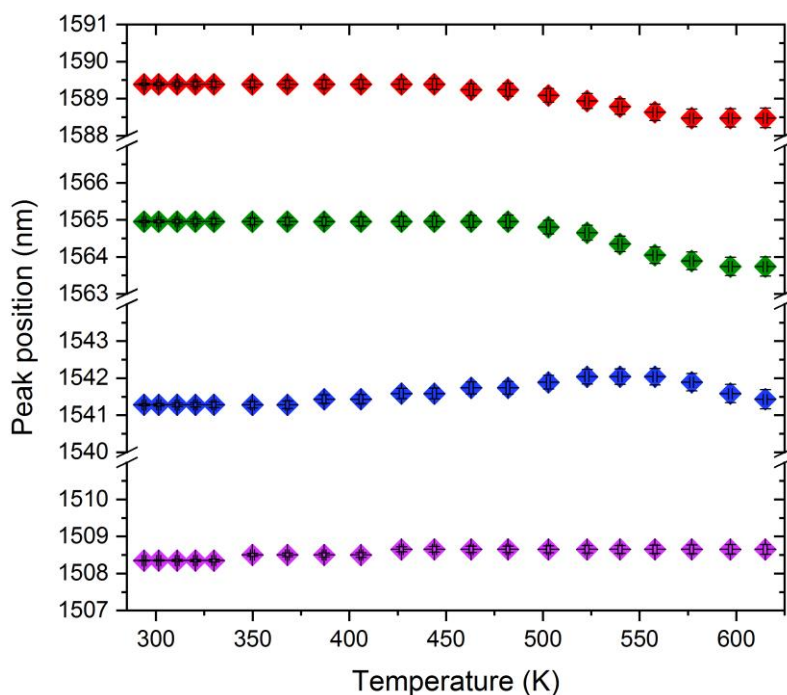
Figure S13. Determined spectral positions of the $^4I_{13/2} \rightarrow {}^4I_{15/2}$ band (four different Stark sublevels centered at $\approx$1508, 1542, 1565 and 1589 nm) of Er^{3+}, as a function of temperature.

References

1   S. Goderski, M. Runowski, P. Woźny, V. Lavín and S. Lis, *ACS Appl. Mater. Interfaces*, 2020, **12**, 40475–40485.

2   H. Suo, X. Zhao, Z. Zhang and C. Guo, *ACS Appl. Mater. Interfaces*, 2017, **9**, 43438–43448.

3   S. Balabhadra, M. L. Debasu, C. D. S. Brites, R. A. S. Ferreira and L. D. Carlos, *J. Phys. Chem. C*, 2017, **121**, 13962–13968.

4   S. K. Singh, K. Kumar and S. B. Rai, *Sens. Actuators A Phys.*, 2009, **149**, 16–20.

5   D. Manzani, J. F. D. S. Petruci, K. Nigoghossian, A. A. Cardoso and S. J. L. Ribeiro, *Sci. Rep.*, 2017, **7**, 1–11.

6   K. Li, D. Zhu and H. Lian, *J. Alloys Compd.*, 2020, **816**, 152554.

7   A. Pandey, V. K. Rai, V. Kumar, V. Kumar and H. C. Swart, *Sensors Actuators, B Chem.*, 2015, **209**, 352–358.

8   H. Lu, H. Hao, Y. Gao, G. Shi, Q. Fan, Y. Song, Y. Wang and X. Zhang, *J. Lumin.*, 2017, **191**, 13–17.

9   E. Pan, G. Bai, L. Wang, L. Lei, L. Chen and S. Xu, *ACS Appl. Nano Mater.*, 2019, **2**, 7144–

7151.

10   M. Runowski, P. Woźny, S. Lis, V. Lavín and I. R. Martín, *Adv. Mater. Technol.*, 2020, **5**, 1901091.

11   K. Soler-Carracedo, I. R. Martin, M. Runowski, L. L. Martín, F. Lahoz, A. D. Lozano-Gorrín and F. Paz-Buclatin, *Adv. Opt. Mater.*, 2020, **8**, 2000678.

12   H. K. Mao, J. Xu and P. M. Bell, *J. Geophys. Res.*, 1986, **91**, 4673–4676.

13   J. D. Barnett, S. Block and G. J. Piermarini, *Rev. Sci. Instrum.*, 1973, **44**, 1–9.

14   M. A. Antoniak, S. J. Zelewski, R. Oliva, A. Żak, R. Kudrawiec and M. Nyk, *ACS Appl. Nano Mater.*, 2020, **3**, 4209–4217.

15   H. Arashi and M. Ishigame, *Jpn. J. Appl. Phys.*, 1982, **21**, 1647–1649.

16   N. J. Hess and G. J. Exarhos, *High Press. Res.*, 1989, **2**, 57–64.

17   Y. R. Shen and W. B. Holzapfel, *Phys. Rev. B*, 1995, **51**, 15752–15762.

18   F. Datchi, R. LeToullec and P. Loubeyre, *J. Appl. Phys.*, 1997, **81**, 3333–3339.

19   M. Runowski, P. Woźny, V. Lavín and S. Lis, *Sensors Actuators B Chem.*, 2018, **273**, 585–591.

20   Y. Wang, T. Seto, K. Ishigaki, Y. Uwatoko, G. Xiao, B. Zou, G. Li, Z. Tang, Z. Li and Y. Wang, *Adv. Funct. Mater.*, 2020, **30**, 2001384.

21   M. Runowski, A. Shyichuk, A. Tymiński, T. Grzyb, V. Lavín and S. Lis, *ACS Appl. Mater. Interfaces*, 2018, **10**, 17269–17279.

22   M. Runowski, P. Woźny, N. Stopikowska, Q. Guo and S. Lis, *ACS Appl. Mater. Interfaces*, 2019, **11**, 4131–4138.

23   M. Runowski, J. Marciniak, T. Grzyb, D. Przybylska, A. Shyichuk, B. Barszcz, A. Katrusiak and S. Lis, *Nanoscale*, 2017, **9**, 16030–16037.